Evolution of Thermoelectric and Oxidation Properties in Lu Substituted Yb₁₄MnSb₁₁

Andrew P. Justl, Sabah K. Bux, and Susan M. Kauzlarich Department of Chemistry, One Shields Ave, University of California, Davis, CA 95616 USA Thermal Energy Conversion Technologies Group, Jet Propulsion Laboratory, California Institute of Technology, 4800 Oak Grove Drive, MS 277-207, Pasadena, CA 91109

*Corresponding author's email: smkauzlarich@ucdavis.edu

Abstract

Yb₁₄MnSb₁₁ is one of the state-of-the-art high temperature p-type thermoelectric materials with reported zTs of 1.2-1.3 at 1273 K. Site substitution of Yb₁₄MnSb₁₁ provides a means to control carrier concentration and impacts the oxidation kinetics. Substitution of Lu³⁺ for Yb²⁺ in Yb₁₄MnSb₁₁ single crystals has been shown to provide faster oxidation kinetics compared with the pristine phase and it has been speculated that this may lead to surface passivation. Polycrystalline samples of Yb_{14-x}Lu_xMnSb₁₁ were synthesized from the elements and through a route utilizing YbH₂, MnSb, and Yb₄Sb₃ as reactive precursors. The solubility of Lu was found to be less than x = 0.5 and at that composition and above LuSb impurities are observed in the powder X-ray diffraction. Because Lu³⁺ is substituting for Yb²⁺ in a p-type system, there is an increase in both the electrical resistivity and Seebeck coefficient with Lu substitution. As Yb₁₄MnSb₁₁ has been predicted to be optimally doped ~1.5 x 10^{21} h⁺ cm⁻³, this reduction in carrier concentration in the solid solution of Yb_{14-x}Lu_xMnSb₁₁ decreases the peak zT. Oxidation of Yb₁₃₋₇Lu_{0.3}MnSb₁₁ as a function of temperature was studied. At low temperatures, the Lu substituted sample may have improved oxidation resistance through forming a passivating oxide film on the surface.

Keywords: Zintl, 14-1-11, oxidation kinetics, thermoelectrics, Ca₁₄AlSb₁₁, Lu doping

Introduction

As space exploration moves further from the sun, the light experienced by the craft diminishes and solar panels become a less viable option for power. Additionally, the need to mechanically deploy large solar panel arrays after launch can prove problematic.^{1,2} Radioisotope thermoelectric generators (RTG) are completely self-sufficient power generators which consist of no moving parts and have a high level of redundancy within the power generating

components. Because of this they are a robust and viable option for the powering of deep space exploration and have powered crafts such as Curiosity, Voyagers I & II, and Cassini.^{3–5}

At the core of these devices is a radioisotope heat source (typically Pu-238 oxide) which gives off a large amount of heat as the radioisotope decays. Around this heated core, a series of p- and n-type thermoelectric materials are used to harness that heat and convert it to electricity. Radiative fins are used on the outside of the device to dissipate waste heat and maintain the cold side of the thermal gradient required for the Seebeck effect to take place within the thermoelectric materials. This is the creation of an electrical potential due to the thermal gradient applied to the material and is quantified by the Seebeck coefficient (S). This is used in combination with the thermal conductivity (κ), and electrical resistivity (ρ) to determine the thermoelectric efficiency of a material which is judged by its unitless figure of merit, $zT = S^2T/\kappa$

Yb₁₄MnSb₁₁ is a complex Zintl phase which crystalizes in the tetragonal *I*4₁/*acd* unit cell shown below in Figure 1. It contains 8 formula units. Each formula unit can be described by the Zintl formalism as containing 13 Yb²⁺, 1 Yb³⁺, 1 [MnSb₄]¹⁰⁻, 1 Sb₃⁷⁻ linear unit, and 4 Sb³⁻. However, magnetism and XANES measurements have shown that there is near negligible Yb³⁺ content within this system, making it electron deficient and a heavily doped p-type material.⁶ The large, complex unit cell lends itself to low thermal conductivities while the high symmetry of the crystal structure leads to degenerate bands and a high density of states near the valence band edge.⁷⁻¹⁰ The high free carrier concentration gives these materials low electrical resistivity while the high density of states near the Fermi level helps to boost Seebeck coefficients through high valley degeneracy. All this combines to make Yb₁₄MnSb₁₁ a state of the art high temperature thermoelectric material with *zT*s of 1.2-1.3 at 1273 K and is being considered for the next generation of RTG.¹¹⁻¹⁴ While the performance of these materials are promising, oxidation from small amounts of residual oxygen within the RTG can be extremely detrimental to performance and stability.

Work on the oxidation of rare earth substituted $Yb_{14-x}RE_xMnSb_{11}$ (RE = La - Nd, Sm – Lu) suggested that substitution of $Yb_{14}MnSb_{11}$ with the late rare earth elements may lead to improved oxidation properties through the rapid formation of a highly stable oxide on the surface which could potentially passivate the interior of the sample from further oxidation. ¹⁵ The rare earths

substitute as 3+ cations and therefore reduce the carrier concentration, impacting the thermoelectric properties. ^{16–18} In contrast to this, a report on Lu substituted Yb₁₄MnSb₁₁ suggested that the carrier concentration increases with increasing amounts of Lu, prompting a reinvestigation of the solid solution to better understand these results. ¹⁹ Investigation of the Ce substituted Yb₁₄MnSb₁₁ shows significant air-stability at room temperature with no oxidation until 430°C and provides a slightly better average *zT*. ²⁰ We have studied the oxidation of Yb₁₄MnSb₁₁ and have shown that it oxidizes with the sublimation of antimony oxides and forms Yb₂O₃ on the surface and YbSb₂ at ~ 800 °C which extrudes from the sample along with the presence of YbMnSb₂. ²¹ This work investigates the synthesis, thermoelectric, and oxidation properties of polycrystalline Yb_{14-x}Lu_xMnSb₁₁. The case of Lu substitution was chosen for the oxidation study as it was expected that the mixed (Yb,Lu)₂O₃ might provide the most stable oxide coating as a previous study showed that Yb_{13.7}Lu_{0.3}MnSb₁₁ formed a oxide scale at ~500 °C that appear to passivate the sample. ¹⁵

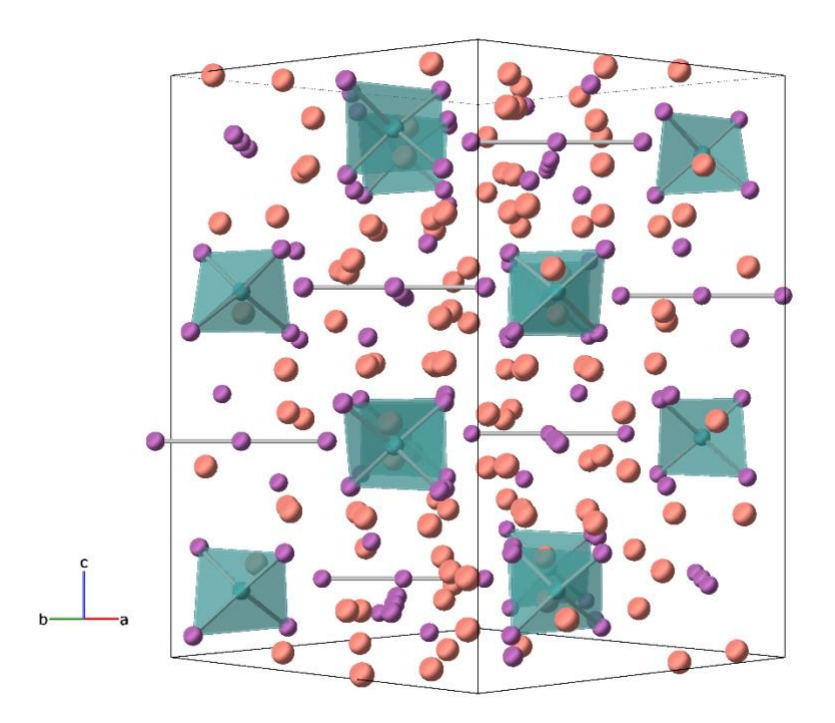


Figure 1. A view of the tetragonal I4_{1/acd} unit cell of Yb₁₄MnSb₁₁ down the [1 1 0] plane. Here, Yb is in orange, Sb is in purple, and Mn is in dark cyan.

Experimental

Synthesis of Yb_{14-x}Lu_xMnSb₁₁ from the elements: Polycrystalline samples of Yb_{14-x}Lu_xMnSb₁₁ (x = 0.3 - 0.7) were prepared by mechanochemical reaction followed by spark plasma sintering (SPS) in 10 g batches utilizing 5% excess in Mn. 12,22 In an Ar filled glovebox (<0.5 ppm O₂), Mn pieces (Alfa Aesar, 99.95%) and Sb shot (Alfa Aesar, 99.999%) were combined in a stainless steel canister with two 11 mm diameter (~8 g) balls (SPEX) and hermetically sealed with an Viton O-ring. The mixture was milled for 1 hour, after which it was pumped back into the Ar filled glovebox. Lu turnings (Edgetech, 99.99%) were then added to the cannister and it was milled for an additional 30 min, after which it was pumped back into the glovebox. Last, Yb turnings (Edgetech, 99.99%) were added to the canister and the mixture was milled for 30 min. The canister was returned to the glovebox and the powder scraped from the canister using a chisel and transferred to a 12.7 mm diameter graphite SPS die with many (15-20) layers of graphite foil between the plungers and the internal sample powder. The reaction was transferred to the chamber of a spark plasma sintering (SPS) instrument. The sample was heated to 1200 °C and 80 MPa of force was applied. After 30 minutes, dense pellets of Yb_{14-x}Lu_xMnSb₁₁ were obtained. The pellets were found to be > 98% dense or greater of theoretical values employing the Archimedes method with toluene as the liquid.

Synthesis of $Yb_{14-x}Lu_xMnSb_{11}$ from binary phases: The most promising composition (x = 0.3) was also synthesized using the route recently developed for $Yb_{14}MnSb_{11}$ which utilizes binary precursors, YbH_2 , Yb_4Sb_3 , and MnSb, to make high purity $Yb_{14}MnSb_{11}$ from stoichiometric reactions. In order to prepare the Lu substituted samples, some of the YbH_2 was replaced by Lu metal.

MnSb was made in a 5 g batch by ball milling followed by annealing as opposed to from the melt as previously described.¹¹ This route can provide MnSb without Sb impurities as there is no crossing of the liquidous line and the reaction is annealed in a region where the full phase width is accessible. Mn pieces (Fisher Scientific, 99.95%) and Sb shot (5NPlus, 99.999%) were added to a 65 cm³ stainless steel grinding canister with two 12.7 mm diameter stainless steel balls (SPEX) in an Ar filled glovebox (<0.5 ppm O₂). The canister was closed and sealed in mylar before being removed from the glovebox. The reaction mixture was milled for two rounds of 1 hour with a 15-minute break in between to help dissipate heat. The canister was brought into the glovebox and the powder was transferred to a Nb tube which was sealed at one end. The other end was then welded shut under Ar. The sealed Nb tube was jacketed in fused silica under

vacuum to prevent oxidation. The reaction was annealed for 12 hours at 750 °C. The reaction was brought into a glovebox and the resultant grey powder was removed from the Nb tube. A small portion was taken for powder X-ray diffraction which showed pure phase MnSb with no unindexed reflections. A typical PXRD pattern can be found in the Supporting Information (SI), Figure S1.

Yb₄Sb₃ was made in 10 g batches as previously described. ¹¹ In brief, in an Ar filled glovebox (<0.5 ppm O₂) Yb metal (Stanford Materials, 99.99%) was cut into small (< 27 mm³) pieces and Sb shot (5NPlus, 99.999%), ground using a mortar and pestle, were added according to stoichiometry to a 55 cm³ tungsten carbide grinding canister (SPEX) with two 11.2 mm diameter tungsten carbide balls. The canister was closed and sealed in Mylar before being removed from the glovebox. It was milled for three rounds of 30 min with scraping using a chisel inside the glovebox in between rounds. The powder was removed from the canister using the chisel and transferred to a Nb tube which was sealed at one end. The Nb tube was sealed with an Argon arc welder and further jacketed in a fused silica tube under vacuum to prevent oxidation. The reaction was then heated to 850 °C and held there for 12 hours. The resultant black powder was removed from the Nb tube under inert atmosphere, and a small portion was taken for powder Xray diffraction. This shows the powder to be a mixture of Yb₄Sb₃ and a small amount of Yb₁₁Sb₁₀ which is the adjacent Yb-deficient phase to Yb₄Sb₃ on the phase diagram. This is a result of small amounts of Yb loss due to cold welding to the canister and is hard to avoid. Because the powder can be represented as a single point in phase space, it is assumed that the Yb₁₁Sb₁₀ is homogenously distributed among the Yb₄Sb₃, and the powder can be treated as one with a single, relatively homogenous elemental composition. A typical PXRD pattern can be seen in (SI), Figure S2.

From a Rietveld refinement of the Yb₄Sb₃ powder, we can solve the final reaction to form Yb_{14-x}Lu_xMnSb₁₁. Similar to what was employed to make the undoped Yb₁₄MnSb₁₁, a three variable, three equation system of equations can be used to solve for the coefficients in equation 1 below.¹¹

x Lu + a YbH₂ + b Yb₄Sb₃ + c Yb₁₁Sb₁₀ + MnSb
$$\rightarrow$$
 Yb_{14-x}Lu_xMnSb₁₁ (Equation 1)
a + 4b + 11c = 14-x (Equation 2)
3b + 10c + 1 = 11 (Equation 3)

$$\frac{b}{\chi_{Yb_4Sb_3}} = \frac{c}{\chi_{Yb_{11}Sb_{10}}}$$
(Equation 4)

Equation 1. The chemical reaction to form $Yb_{14-x}Lu_xMnSb_{11}$ from Lu, YbH_2 , and Yb_4Sb_3 with $Yb_{11}Sb_{10}$ impurities. Equations 2-4: The three equations used to solve for the variables in equation 1. Equation 2 is used to set the Yb + Lu content to 14 where x is the desired x value for Lu in $Yb_{14-x}Lu_xMnSb_{11}$ and needs to be predetermined. Equations 3 sets Sb content to 11. Equations 4 uses the results from Rietveld refinement of the Yb_4Sb_3 powder which is then converted into mole fractions (χ , chi) of Yb_4Sb_3 and $Yb_{11}Sb_{10}$ which are denoted by their respective subscripts.

Using equations 2-4 and the results from the Rietveld refinement of the Yb₄Sb₃ powder, the variables within equation 1 can be solved to get the desired balanced reaction. Beginning with equation 4, both mole fractions are known values from the refinement, so that equation can be rearranged to substitute for either variable within equation 3. Once one variable is solved, the other is easily obtained which allows for solving of equation 2. Once all variables are obtained, they can be inserted into equation 1 to get the balanced chemical reaction to form Yb₁₄_xLu_xMnSb₁₁ from Lu, YbH₂, MnSb, and Yb₄Sb₃ (with or without Yb₁₁Sb₁₀ impurities).

Once the above equations were solved and the chemical reaction was obtained, reactions were calculated using a 5 g total mass. The masses of Yb₄Sb₃ and Yb₁₁Sb₁₀ were recombined as that is a representation of the single powder source which is Yb₄Sb₃ with the respective mole fraction of Yb₁₁Sb₁₀. In an Ar filled glovebox, a small piece of Lu (Alfa Aesar, 99.9%) was put into a pair of locking plyers and then the fine side of a file was used to process the Lu into fine filings which were collected on aluminum foil below the file. The Lu filings were then added to a 65 cm³ stainless steel grinding canister with two 12.7 mm balls. YbH₂ (American elements, 99.999%), originally purchased as powdered Yb metal but determined to be the hydride by PXRD (SI Figure S3), was then added along with the Yb₄Sb₃ and MnSb binary powders which had previously been prepared. The canister was sealed in Mylar and milled for 3 rounds of 30 minutes with a 180° flip in the mill after the first round and a scrape using a chisel in the glovebox after the second. The reaction mixture was then brought into the glovebox, removed from the canister, and was transferred to a 12.7 mm diameter graphite SPS die (CalNano). The die was then placed in the chamber of a SPS instrument (Dr. Lab Sinter Jr., Fuji Corp.) and the chamber was evacuated (<13 Pa). Initially, the force is set to 5 kN and the reaction is heated to

600 °C where it is held for 30 minutes. During this time, the off-gassing of the hydrogen from the decomposition of the YbH₂ can be seen if pressure is being monitored and can be used to see the progress of the reaction. After 30 minutes under active vacuum, the pressure of the chamber will have returned to starting values. After this time the reaction was ramped to 850 °C to facilitate sintering and consolidation. During this step, the force was increased to 6.5 kN upon beginning to change temperature. The reaction was held at this elevated temperature and pressure stage for 20 minutes which results in high density (>98%), high purity Yb_{14-x}Lu_xMnSb₁₁. This was confirmed by PXRD and EDS.

Powder X-ray Diffraction (PXRD): Powder X-ray diffraction was performed on ground slices of the Yb_{14-x}Lu_xMnSb₁₁ pellets and portions of oxidized samples on a Bruker D8 Advanced Eco or an Aeris Panalytical diffractometer with Cu K_α radiation and a Ni K_β filter. In the case of the Aeris diffractometer the samples were prepared on a silicon zero-background holder. The resultant powder patterns were analyzed using a Rietveld refinement using the Jana2006 software package.²³

Elemental Composition: Elemental composition of Yb_{14-x}Lu_xMnSb₁₁ samples were determined by energy dispersive spectroscopy using a Themo-Fisher Quattro Environmental SEM equipped with a Bruker xFlash 6-100 detector. EDS data were analyzed using Bruker ESPIRIT software and final compositions are an average of 10 points across a selected area. A single crystal of Yb₁₄MnSb₁₁ was used for standardization of Yb, Mn, and Sb.

Thermal Conductivity: Thermal conductivity of Yb_{14-x}Lu_xMnSb₁₁ samples were determined by measuring thermal diffusivity from room temperature to 1000 °C at 50 °C increments with 3 measurements taken at each step. Thermal diffusivity measurements were performed using a Netzsch LFA 457 Microflash under Ar flow on thin slices (<1.5 mm) of the densified Yb_{14-x}Lu_xMnSb₁₁ pellets. Slices were polished until a uniform flat surface was achieved. The density of the disks was determined using the Archimedes method with toluene as the liquid. The heat capacities of the samples of Yb_{14-x}Lu_xMnSb₁₁ were estimated based on the heat capacity of Yb₁₄MnSb₁₁ which was then modified for the molecular weight of the doped compound where C_P(Yb_{14-x}Lu_xMnSb₁₁) = C_p(Yb₁₄MnSb₁₁) × MW(Yb_{14-x}Lu_xMnSb₁₁)/MW(Yb₁₄MnSb₁₁). ^{11,12,24-26} Here, MW stands for the molecular weight of the respective compounds. The thermal expansion of Yb₁₄MnSb₁₁ was used to estimate the temperature dependence of density in the Lu-substituted

compounds. ^{12,14,26} These were all combined to give the total thermal conductivity according to the equation: $\kappa = D \times C_p \times d$ (D = measured diffusivity; C_p = heat capacity adjusted for molar mass; d = the temperature-adjusted density from Yb₁₄MnSb₁₁).

High Temperature Seebeck Coefficient: The Seebeck coefficients of Yb_{14-x}Lu_xMnSb₁₁ samples were measured at JPL on a custom built light pipe instrument with tungsten-niobium thermocouples under high vacuum.²⁷

Hall Measurements and Van der Pauw Resistivity: Electrical resistivity and Hall carrier concentrations were measured were measured at JPL using the Van der Pauw method with a current of 100 mA and a 1.0 T magnet on a specialized high-temperature instrument.²⁸

Thermogravimetry and Differential Scanning Calorimetry (TG/DSC): The thermal stability and oxidation properties of Yb_{14-x}Lu_xMnSb₁₁ were determined using TG/DSC on a Netsch STA 449 F3 Jupiter with samples in Al₂O₃ crucibles. Non-oxidative measurements were performed under a protective flow (20 mL/ min) of ultra-high purity Ar (Praxair, 99.999%) with a polished piece of Zr ribbon placed on top of the heat shield to act as an oxygen getter. Oxidation studies were performed under a flow of dry air (20% O₂, 80% N₂, Praxair, 50 mL/ min). All studies were performed with a heating rate of 10 K/ min. Samples were analyzed using PXRD after TG/DSC measurements. Oxidation studies were repeated an additional time to obtain a second sample which was set in epoxy for SEM/ EDS.

Pellet Oxidation: A sample of Yb_{14-x}Lu_xMnSb₁₁ (x = 0.3) was made by the binary precursor route as described above. After a thin slice was taken from the pellet for PXRD to confirm the purity and phase identity, the thick (\sim 3 mm) pellet was polished flat then placed into an Al₂O₃ crucible where the pellet was supported by 3 Al₂O₃ rods which only contact the pellet on the edges at single points. This helps to minimize any potential reactions between the sample and the Al₂O₃. The sample was then placed into a box furnace and was heated to 1000 °C at a rate of 200 °C/h and held there for 12 hours under ambient atmosphere. The oxidized pellet was then split in half where one half was set into epoxy for SEM/ EDS and the other half was dissected to perform PXRD on the individual components.

Results and Discussion

Synthesis and Phase Purity

Samples of Yb_{14-x}Lu_xMnSb₁₁ were analyzed by PXRD provided in Figure 2. For the pristine sample along with x = 0.3, all reflections are well indexed as the tetragonal Yb₁₄MnSb₁₁ phase with no unaccounted-for intensities. The x = 0.3 samples made from binary precursors showed a small (0.47(4) and 0.99(7) wt%) Yb₂O₃ impurity which was also seen when making pristine Yb₁₄MnSb₁₁ on stoichiometry by the same route.¹¹ As x is increased to 0.5 and above the presence of LuSb can be seen by the presence of the 100% diffraction peak at 29.7° 20 marked by the blue triangle.²⁹ This suggests that there is a limited solubility of Lu within the main Yb₁₄MnSb₁₁ phase. Upon exceeding this point, excess Lu reacts with Sb forming the stable, cubic LuSb impurity. This is in good agreement with studies on single crystals of Yb₁₄-xRExMnSb₁₁ (RE = rare earth) which also saw a limited solubility of trivalent rare earth elements within the Yb₁₄MnSb₁₁ structure.^{15,30} Table 1 provides the phase % and statistics from Rietveld refinement of the PXRD patterns. Full pattern refinements and lattice parameters are provided in Supporting information (SI) Figure S4 and Table S1.

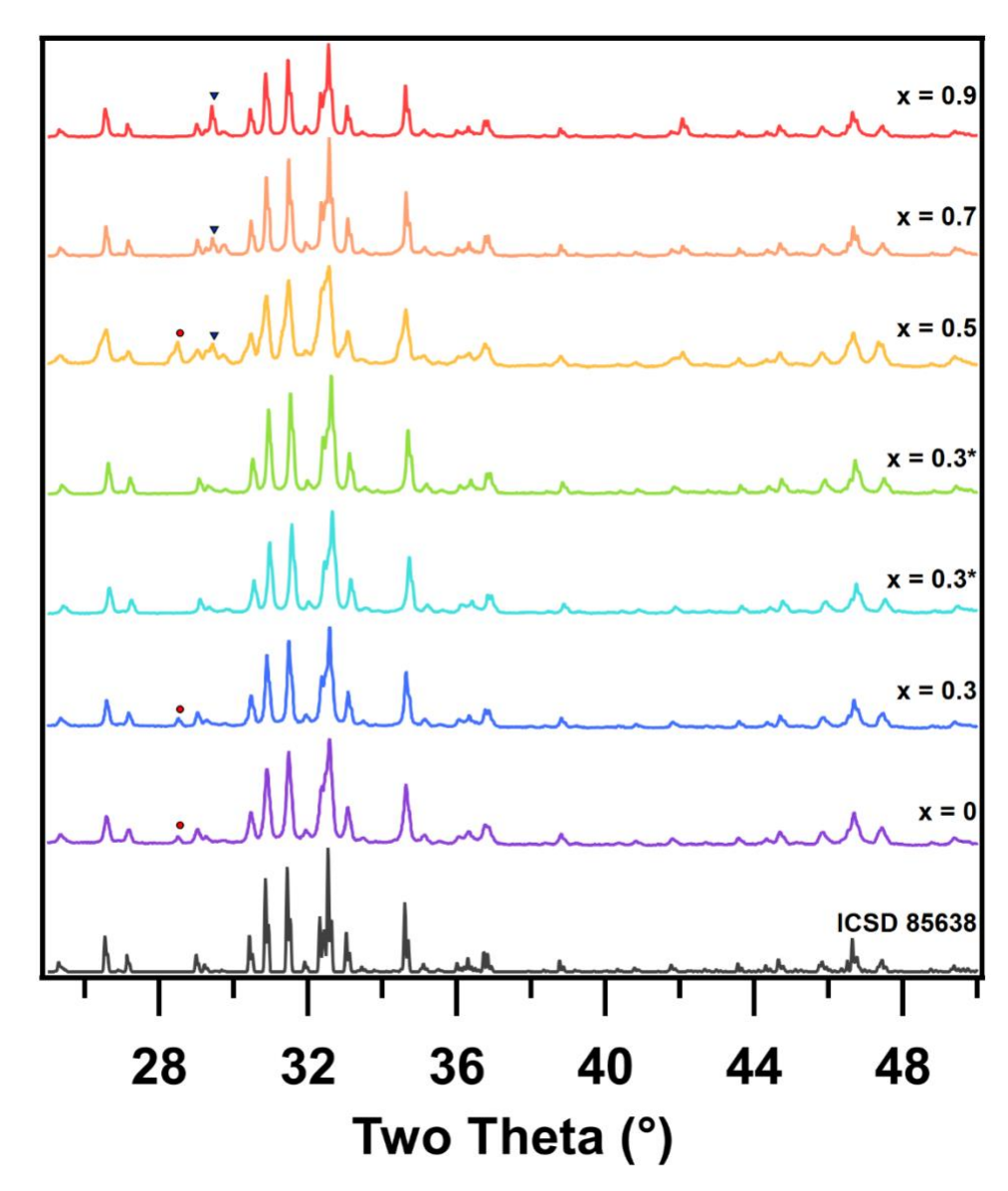


Figure 2. Powder X-ray diffraction patterns of Yb_{14-x}Lu_xMnSb₁₁ with *x* increasing up the *y*-axis. A reference pattern for Yb₁₄MnSb₁₁ with the ICSD number is provided. Si was added to some samples as a standard marked by a red circle. The largest reflection from LuSb is marked by the blue triangle.

Table 1. Results and Statistics from Rietveld Refinement of Yb14-xLuxMnSb11 PXRD

	Yb _{14-x} Lu _x MnSb ₁₁	LuSb	Yb ₂ O ₃	GoF, Rp, wRp
$x = 0^a$	100 wt%	0 wt%	0 wt%	1.44, 3.72, 4.81
$x = 0.3^{a}$	100 wt%	0 wt%	0 wt%	1.40, 4.37, 5.55
$x = 0.3^{b, c}$	99.01(7) wt%	0 wt%	0.99(7) wt%	1.30, 6.51, 8.73
			, ,	

$x = 0.3^{b, d}$	99.57(3) wt%	0 wt%	0.47(4) wt%	1.34, 6.24, 8.49
x = 0.5	94.5(5) wt%	3.74(6) wt%	1.66(6) wt%	2.13, 5.40, 7.28
x = 0.7	93.65(8) wt%	2.85(5) wt%	3.50(7) wt%	1.94, 6.52, 9.15
x = 0.9	91.56(8) wt%	6.80(6) wt%	1.65(7) wt%	1.75, 6.99, 9.17

^aData collected on a Aeris Panalytical diffractometer with a zero background holder.

In addition to PXRD, samples were characterized using scanning electron microscopy (SEM) and energy dispersive spectroscopy (EDS). Backscattered electron micrographs of the Yb_{14-x}Lu_xMnSb₁₁ samples used in the thermoelectric studies can be seen in Figure 3. The sample of Yb₁₄MnSb₁₁ made from the elements (Figure 3a)) shows no major deviations in contrast which suggests a high degree of homogeneity. The sample of x = 0.3 made from the elements (Figure 3b)) shows notable clusters of particles which have deviations in contrast in comparison to the main phase consistent with a side phase, likely LuSb, present within the main matrix. In the sample of x = 0.3 made from Lu, YbH₂, Yb₄Sb₃, and MnSb (Figure 3c)) there are no regions which show significant contrast suggesting relative phase purity in comparison to the sample made from the elements. As Lu is increased to x = 0.5 (Figure 3d)), the sample shows even contrast across the whole matrix, suggesting that the LuSb side phase seen by PXRD is well distributed across the matrix. At x = 0.7 (Figure 3e)), the small dark spots within the main matrix can be seen much like that for the x = 0.3 sample made from the elements and are agglomerating into larger (~10 µm) continuous features. At x = 0.9 (Figure 3f)), these darker regions have become larger and more numerous which agrees with the larger amounts of LuSb seen in PXRD.

^b Synthesized from binaries and Lu, as described below.

^c Sample for the oxidation study, as described below.

^d Thermoelectric properties measured.

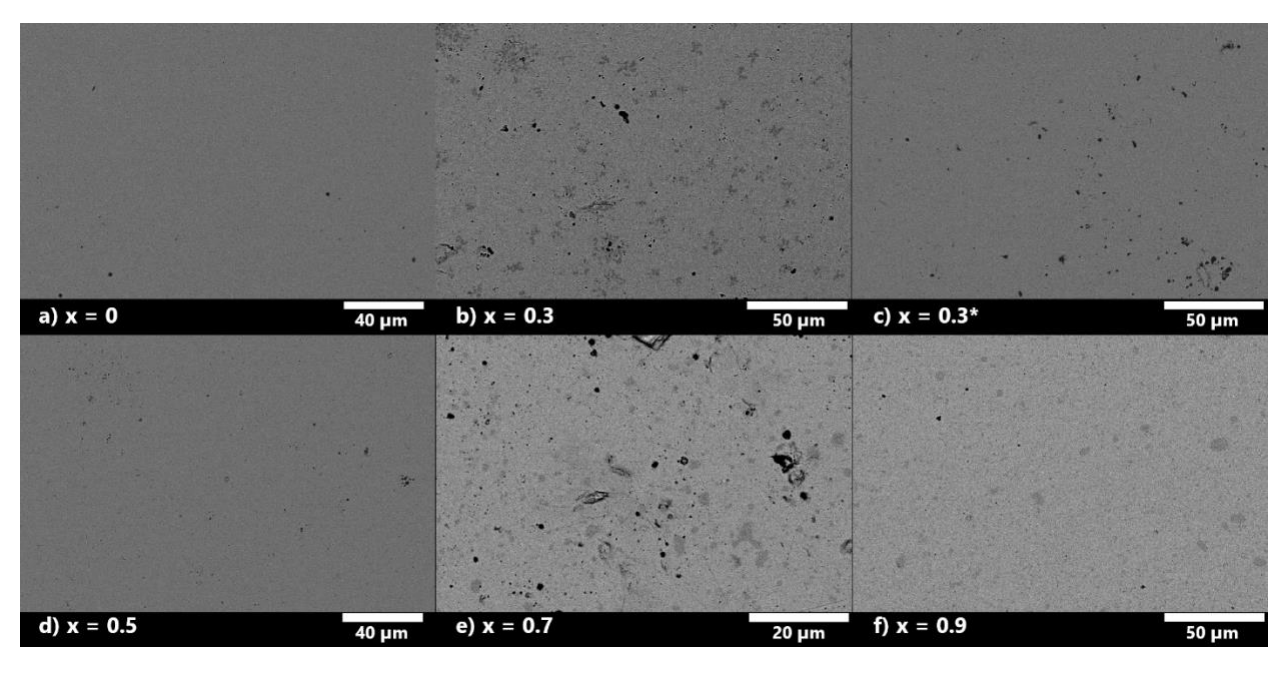


Figure 3. Backscattered electron micrographs of Yb_{14-x}Lu_xMnSb₁₁ samples used in thermoelectric property measurements. The sample of x = 0.3 made by the binary route is noted by an asterisk (*). All other samples were made from the elements. Note that the scale bar is 20 μ m for x = 0.7 sample micrograph to better show the inclusions.

Table 2 shows the results (an average from 10 points) from energy dispersive spectroscopy on samples of Yb_{14-x}Lu_xMnSb₁₁. The sample of Yb₁₄MnSb₁₁ is close to the nominal stoichiometry, however Yb appears to be slightly deficient, and Sb slightly rich. This may be attributed to the generally lower accuracy of EDS in comparison to a more quantitative technique such as electron probe micro analysis (EPMA/ Microprobe) especially when emission peaks begin to overlap.³¹ Looking at the composition of the Lu doped samples, it can be seen that in all cases, the amount of Lu detected is less than nominal with the discrepancies becoming more pronounced at higher Lu content. In addition to deviations from the nominal, the higher Lu content samples also show higher internal deviations in the Lu content across the sample. This agrees with the inhomogeneous sample matrix seen in backscattered electron micrographs.

Table 2. Analysis of Energy Dispersive Spectroscopy for Pellets of Yb_{14-x}Lu_xMnSb₁₁

	Lu (at%)	Yb (at%)	Mn (at%)	Sb (at%)	
Sample	Experimental				

	Nominal				
x = 0	0	52.3(3)	3.94(18)	43.8(2)	
	0	53.8	3.85	42.3	
x = 0.3	0.70(13)	51.5(3)	3.86(21)	43.9(5)	
	1.2	52.7	3.85	42.3	
x = 0.3*	0.45(8)	51.9(2)	3.98(15)	43.7(2)	
	1.2	52.7	3.85	42.3	
x = 0.5	0.83(16)	51.3(3)	3.99(21)	43.9(2)	
	1.9	51.9	3.85	42.3	
x = 0.7	1.05(92)	52.1(4)	3.92(17)	42.9(1.1)	
	2.7	51.2	3.85	42.3	
x = 0.9	1.74(1.59)	49.3(3.5)	3.80(1.11)	45.1(2.9)	
	3.5	50.4	3.85	42.3	

^{*}Sample prepared from binaries and Lu (see Table 1).

Thermoelectric Properties

Thermal Conductivity, Electrical Resistivity & Transport

Figure 4 shows the thermal conductivity, electrical resistivity, Seebeck coefficient and zTof the Yb_{14-x}Lu_xMnSb₁₁ series. Thermal conductivity (Figure 4a)), resistivity (Figure 4b)), and Seebeck coefficients (Figure 4c)) follow similar profiles to previously published literature on the light rare earth substitutions. ^{20,30} The previously published thermal conductivity of Yb₁₄-_xLu_xMnSb₁₁ does not follow this trend. ¹⁹ In general, the thermal conductivity shown in Figure 4a) is reduced due to alloy scattering and a lowering of the electronic component, while the electrical resistivity and Seebeck coefficients are increased due to reduction in carrier concentration from the substitution of Lu³⁺ for Yb²⁺. The thermal conductivity of the sample of Yb₁₄MnSb₁₁ begins at 8.4 mW cm⁻¹K⁻¹ at room temperature, increases to a maximum of 8.9 mW cm⁻¹K⁻¹ at 573 K due to an increase in electronic contribution as carriers move between the bands of the complex structure. 9 After this point, phonon scattering dominates and there is a decrease in the thermal conductivity to a minimum of 7.7 mW cm⁻¹K⁻¹ at 1073 K. As the temperature increases, there is an upturn in the thermal conductivity which corresponds to the onset of bipolar conduction and an increase electronic contribution due to the activation of minority carriers. 9,11,24,25 This agrees well with previously reported thermal conductivities of polycrystalline samples of Yb₁₄MnSb₁₁ made from both elemental and binary precursors. 11,12 The temperature dependent behavior of this sample (x = 0.9) is distinct and likely a result of increased contributions from the larger amounts of LuSb impurity seen in both PXRD and SEM.

LuSb is also seen in the PXRD and SEM for x = 0.7 at lesser amounts and may explain the trend of increasing thermal conductivity at x = 0.7 and 0.9. The sample of x = 0.5 also has LuSb present (3.74(6) wt%) seen in the PXRD, however, the inclusions were not easily seen in backscattered electron micrographs suggesting they are small and well distributed throughout the matrix. Table 3 provides the values for the room temperature value of thermal conductivity, along with maximum and minimum and corresponding temperatures. The trend follows as expected, with reduction in the thermal conductivity due to alloy scattering and shift in the temperatures for the initial bend over and thermal conductivity minimum due to the shifting of the Fermi level. There are slight differences between the x = 0.3 sample made with elements vs. binaries that is likely attributed to a slight difference in composition.

Table 3. Thermal Conductivity and Electrical Resistivity at Temperature for Yb_{14-x}Lu_xMnSb₁₁

Yb _{14-x} Lu _x MnSb ₁₁	Thermal Conductivity (mW cm ⁻¹ K ⁻¹)			Electrical Resistivity (mΩ·cm)	
x	κ _{RT}	κ _{max} (T)	κ _{min} (T)	ркт	ρ _{max} (T)
0	8.4	8.9 (573 K)	7.7 (1073 K)	1.89	5.98 (1260 K)
0.3*	8.2	8.5 (523 K)	7.3 (1073 K)	1.90	6.07 (1260 K)
0.3	8.5	8.7 (473 K)	7.6 (1073 K)	2.10	7.20 (1260 K)
0.5	8.1	8.3 (425 K)	7.1 (1023 K)	2.32	8.07 (1253 K)
0.7	7.7	7.7 (375 K)	6.4 (873 K)	2.73	9.95 (1220 K)
0.9	8.4	8.4 (298 K)	7.1 (973 K)	2.24	7.48 (1171 K)

^{*} made from binary precursors

The electrical resistivity shown in Figure 4b) of Yb₁₄MnSb₁₁ begins at 1.89 m Ω ·cm at room temperature and increases to a maximum of 5.98 m Ω ·cm at 1260 K. The Seebeck coefficients of all samples start at the same approximate room temperature value between 40 - 47 μ V K⁻¹ with the major differences becoming apparent as temperatures increase. The exception is the x = 0.3 made by binaries where the electrical resistivity is like that of the pristine sample.

The sample of x = 0.9 shows an electrical resistivity between that of x = 0.5 and x = 0.3. This sample had a room temperature resistivity of 2.24 m Ω ·cm and a maximum of 7.48 at 1171 K. The lowered electrical resistivity of this sample is likely due to contributions from the LuSb impurities which has been shown to be semi-metallic with low electrical resistivity through

experimental and computational methods.³² It is likely that the previous report provided Yb₁₄- $_x$ Lu $_x$ MnSb₁₁ contaminated with other phases as the resistivity trends and carrier concentration do not follow expectations based on the band structure. Therefore, those results will not be compared as they are not relevant to this work.¹⁹ Hall carrier centration and mobility is provided in SI, Figure S6 and Table S2 and are consistent with the resistivity data.

The sample of Yb₁₄MnSb₁₁ reaches a maximum of 221.9 μ V K⁻¹ at 1265 K (Figure 4c)) with no turn-over at the highest temperature ranges and reaches a peak zT of 1.26 at 1225 K (see Figure 4d) and Table 4). This peak value matches well with the best samples of Yb₁₄MnSb₁₁ although the peak comes at a slightly earlier temperature than what has been previously reported (1225 K vs. 1275 K). The earlier peak in zT may be due to a slight off-stoichiometry in Yb which has been shown to effect the thermoelectric performance of this phase in the highest temperature range. The earlier peak is zT may be due to a slight off-stoichiometry in Yb which has been shown to effect the thermoelectric performance of this phase in the highest temperature range.

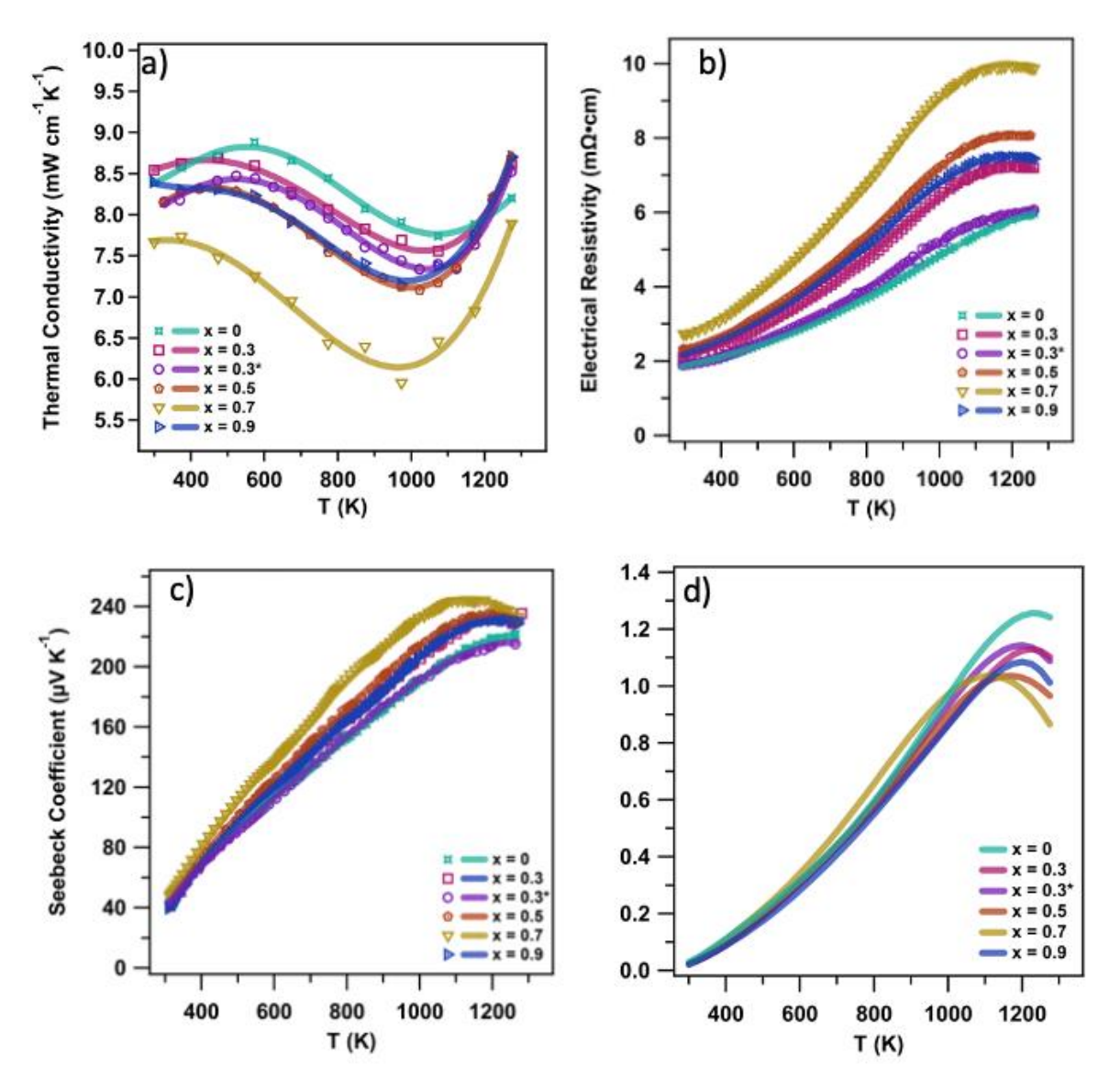


Figure 4. Temperature dependent a) thermal conductivity b) electrical resistivity, c) Seebeck coefficient, and d) zT of the Yb_{14-x}Lu_xMnSb₁₁ series. The markers are data at the given temperature and the solid lines are the polynomial fits used for zT calculations. The sample of x = 0.3 made from binary precursors is marked by an asterisk in the legend.

The temperature dependent Seebeck coefficients of the Yb_{14-x}Lu_xMnSb₁₁ series are provided in Figure 4c) and Table 4. As Lu is increased to x = 0.3, the sample made from the binary precursors reaches a maximum of 217.68 μ V K⁻¹ at 1224 K before bending over due to bipolar conduction. The sample of x = 0.3 made from the elements reached a larger peak Seebeck coefficient of 232.14 μ V K⁻¹ at 1217 K before bending over. At x = 0.5, the peak Seebeck

coefficient reached increased to 235.45 µV K⁻¹ at 1188 K after which the Seebeck coefficient decreases. This trend of increasing Seebeck coefficient and decreasing bend-over temperature continues with x = 0.7 which reaches a peak of 244.45 μ V K⁻¹ at 1128 K. The sample of x = 0.9deviates from this trend with a lower peak Seebeck coefficient of 231.56 µV K⁻¹ at 1209 K. The trend of increasing Seebeck coefficient and decreasing bend-over temperature (along with Hall data) confirms that the Lu addition is leading to the lowering of the carrier concentration which leads to the Fermi level being closer to the valence band edge. Therefore, the onset of bipolar conduction occurs at lower temperatures as minority carriers need less thermal energy to cross the band gap. This is similar to what is observed for the Yb₁₄Mg_{1-x}Al_xSb₁₁ system where carrier concentrations were manipulated through replacement of Mg²⁺ for Al⁺³ which donates more electrons to the p-type system. Here, Yb²⁺ is being exchanged for Lu³⁺ which leads to a similar effect of lowering the carrier concentration. This is consistent with other rare earth substituted samples of $Yb_{14-x}RE_xMnSb_{11}$ (RE = Pr, Nd, Sm, Gd) where the rare earth substituted samples showed additional electron donation to the p-type system.³⁰ In the example of RE = Ce, the is a slight improvement with increasing amounts of Ce, as the unit cell also increases, thereby impacting the Fermi level.²⁰

Table 4. Seebeck coefficient and Figure of Merit, zT, at Temperature for Yb_{14-x}Lu_xMnSb₁₁

Yb _{14-x} Lu _x MnSb ₁₁	Seebeck coefficient		zT
		$\mu V K^{-1}$	
x	Srt	S _{max} (T)	$zT_{\max}(T)$
0	44.4	221.92 (1264 K)	1.26 (1225 K)
0.3*	43.4	217.68 (1224 K)	1.14 (1200 K)
0.3	41.1	232.14 (1217 K)	1.13 (1225 K)
0.5	44.1	235.45 (1188 K)	1.04 (1175 K)
0.7	47.4	244.45 (1128 K)	1.04 (1100 K)
0.9	39.6	231.56 (1209 K)	1.09 (1175 K)

^{*}made from binary precursors

As Lu is added into the samples, the peak zTs decrease, as shown in Figure 4d). The sample of x = 0.3 made from binary precursors reached a maximum of 1.14 at 1200 K whereas

the samples made from the elements all show even further reduced peak zT values due to the higher electrical resistivity of these samples. Despite this, even the worst performing sample (x = 0.7) had a peak zT of 1.04 at 1100 K, which is still above the zT = 1.0 value that many consider to be the threshold for high performance materials.

Oxidation Studies

High thermoelectric performance in the relevant operating temperature is only one aspect that needs to be considered when considering the implementing of a thermoelectric material into a thermoelectric generator. Oxidation at operating temperatures due to residual oxygen in the generator can be detrimental to the long-term stability of the thermoelectric materials and, in turn, the generator. This makes understanding and improving the oxidation properties of a material important. Although the $Yb_{14-x}Lu_xMnSb_{11}$ series all show decreases in figure in merit compared to the $Yb_{14}MnSb_{11}$, work on the oxidation of single crystals of $Yb_{14-x}RE_xMnSb_{11}$ suggested that substitution with the late rare earth elements improves the oxidation properties by quickly forming a stable, passivating oxide shell. As the x = 0.3 sample made from binaries showed similarly high zT compared with $Yb_{14}MnSb_{11}$, this sample was chosen for investigation into the oxidation properties.

A piece from the other half of the same Yb_{13.7}Lu_{0.3}MnSb₁₁ pellet used for thermoelectric measurements was measured using thermogravimetry and differential scanning calorimetry (TG/DSC) under a flow of Ar to 1100°C (Figure 5a)) to establish a baseline and under a flow of dry air (20% O₂ in N₂) to 1000°C (Figure 5b)). To confirm the changes under the dry air flow, two different pieces from the pellet were measured, as indicated in Figure 5b). The baseline TG measurement shows a very small mass gain over the course of the measurement due to residual oxygen within the system. The TG of both pieces under the dry air flow show a large mass gain which onsets at 460°C and starts to level off as temperature increases. Upon cooling, the samples showed a relatively stable mass, only increasing by 0.15 – 0.17%. The DSC shows a sweeping exotherm on heating due to the minor oxidation of the sample. After the TG/DSC measurement, PXRD showed only a small amount of oxide in addition to the main phase (Rietveld refinement results: 2.21(11) wt% Yb₂O₃ with GoF: 1.53, Rp: 7.36, wRp: 10.66). The DSC curves of the two pieces under flowing dry air show a small sweeping exotherm which increases steadily until 400°C. At that point, there is a large exotherm which peaks around 613 - 629°C. At 740 - 749°C

there is a small exotherm along with a larger endotherm at 783 - 786°C. In the oxidation of the first piece, there is an additional small exotherm at 716°C. Upon cooling there is a sharp exotherm at 750 – 753°C which has a small shoulder at 764 - 765°C. There is also a second small exotherm at 559 - 562°C. As the large exothermic peak which onsets around 400°C corresponds well with the onset of mass increase seen in TG, this event can be attributed to the high temperature oxidation of the Yb_{14-x}Lu_xMnSb₁₁. Because the peak of this high temperature oxidation occurs close to where the rate of mass gain begins to lessen, it is possible that this is due to the formation of a passivating oxide layer which slows the rate of the oxidation reaction in layers below. As there is a small exotherm on heating at low temperatures it is likely that there is oxidation occurring at the surface of the polished Yb_{14-x}Lu_xMnSb₁₁ even at these low temperatures, but the oxide film formed must be passivating enough to prevent significant mass gain. A comparison of the TG/DSC for the oxidation of Yb₁₄MnSb₁₁ and Yb_{14-x}Lu_xMnSb₁₁ is shown in the supporting information (Figure S5).²¹ The DSC of the unsubstituted Yb₁₄MnSb₁₁ shows an additional exothermic peak in the large sweeping exotherm at 550°C which may correspond to the exotherm seen upon cooling in the Lu substituted samples. In addition to this difference, the unsubstituted samples have several sharp exotherms at high temperatures from reactions with the crucible. In the TG both pieces of the Lu substituted material show flatter signals on cooling, suggesting there is an improvement in the passivating capabilities compared to the unsubstituted Yb₁₄MnSb₁₁. Pictures of one of the pieces of Yb_{13.7}Lu_{0.3}MnSb₁₁ Figure 5c) before and Figure 5d) after oxidation in the TG/DSC experiment shown above. Before oxidation, the sample is a polished black material with a shiny surface. After oxidation the sample has formed a continuous brown-black coating which seems to coat the entire surface. In addition to the brown shell, there is a mass of black material seen on the left side of the sample which appears to have melted out of the sample. This is very similar to what was observed for the oxidation of undoped Yb14MnSb11 in both the shell appearance and the melted mass.21

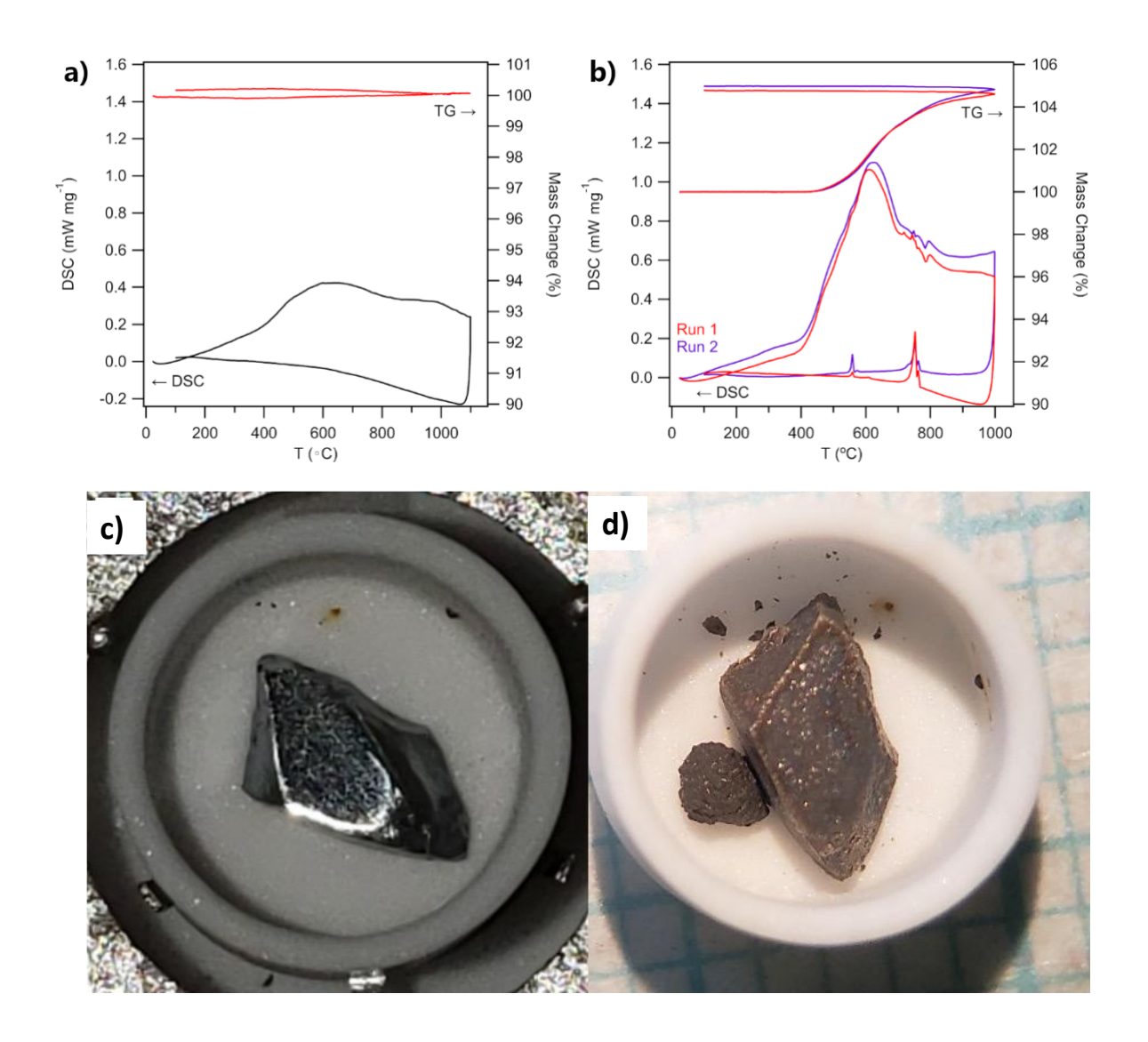


Figure 5. a) The TG/DSC of Yb_{13.7}Lu_{0.3}MnSb₁₁ from room temperature to 1100°C under flowing Ar(g). The DSC is shown on bottom using the left axis and the TG is on the top using the left axis. b) TG/DSC from room temperature to 1000°C under dry air of two different pieces of Yb_{13.7}Lu_{0.3}MnSb₁₁ from the same pellet. The DSC is shown on bottom using the left axis and the TG is on the top using the left axis. Pictures of a piece of Yb_{13.7}Lu_{0.3}MnSb₁₁ c) before and d) after oxidation in a TG/DSC experiment.

To better interpret the series of exo- and endotherms, one of the pieces of Yb₁₄₋ xLu_xMnSb₁₁ was ground for PXRD which can be seen in Figure 6. The diffraction pattern

consists of Yb_{14-x}Lu_xMnSb₁₁, Yb₁₁Sb₁₀, YbSb, YbSb₂, YbMnSb₂, and Yb₂O₃. All but YbSb had previously been identified in the oxidation of pure Yb₁₄MnSb₁₁ made from binary precursors. It is likely that the inclusion of Lu helps to stabilize the formation of the 1:1 phase, as Lu is more stable as a trivalent cation and to achieve charge neutrality the structure requires a trivalent cation to balance the Sb³⁻ anion.

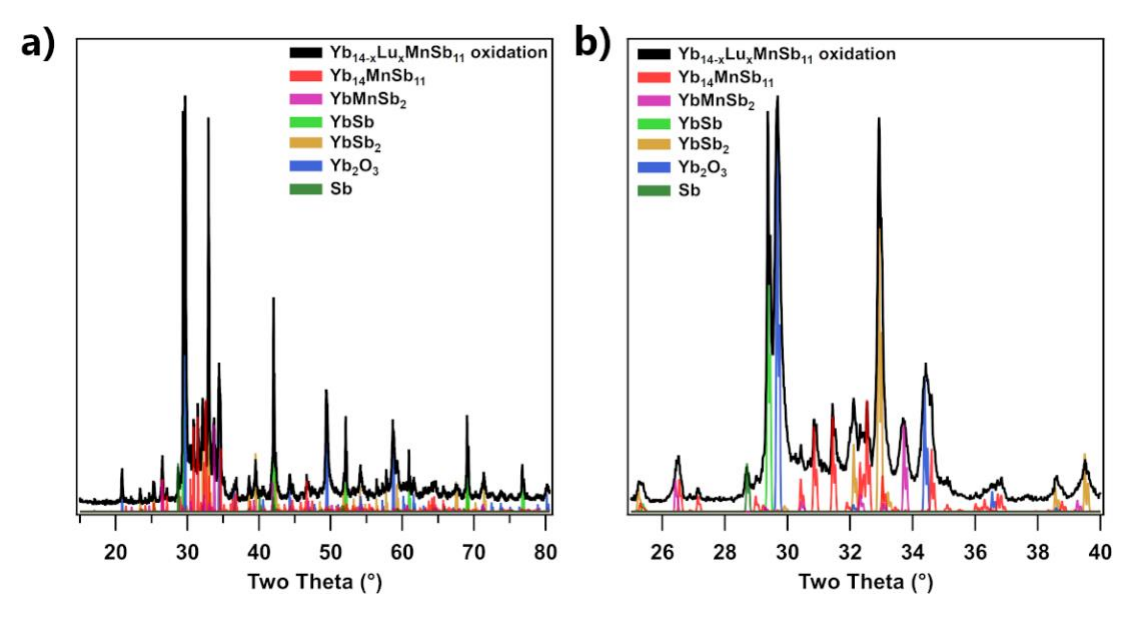


Figure 6. PXRD of a piece of Yb_{13.97}Lu_{0.3}MnSb₁₁ after oxidation in a TG/DSC experiment. a) shows the full range of two theta and b) an enlarged two theta view of the region where many of the strong reflections occur.

In addition to PXRD, the other piece of Yb_{13.7}Lu_{0.3}MnSb₁₁ was set into epoxy and sanded to reveal the cross section. This was then analyzed using scanning electron microscopy which can be seen in Figure 7. The backscattered electron micrographs show the sample to consist of an outermost dark shell which extends about $20 - 50 \mu m$ below the surface. This shell looks to be continuous with only small amounts of cracking. Inside of that is a lighter region of the shell which extends another $70 - 100 \mu m$ into the sample. No cracking appears to extend beyond this region, but there is some porosity. Inside of this region is a porous void space. This is potentially where the melted material once was before becoming liquidous and breaking through the outer shell. Interior to this void region is a more porous region which surrounds a solid core which shows no porosity or variance in contrast. The backscattered micrograph of the ball of melted

material which was found on the outside of the material reveals a striated contrast pattern which may be indicative of a eutectic melt which has solidified.

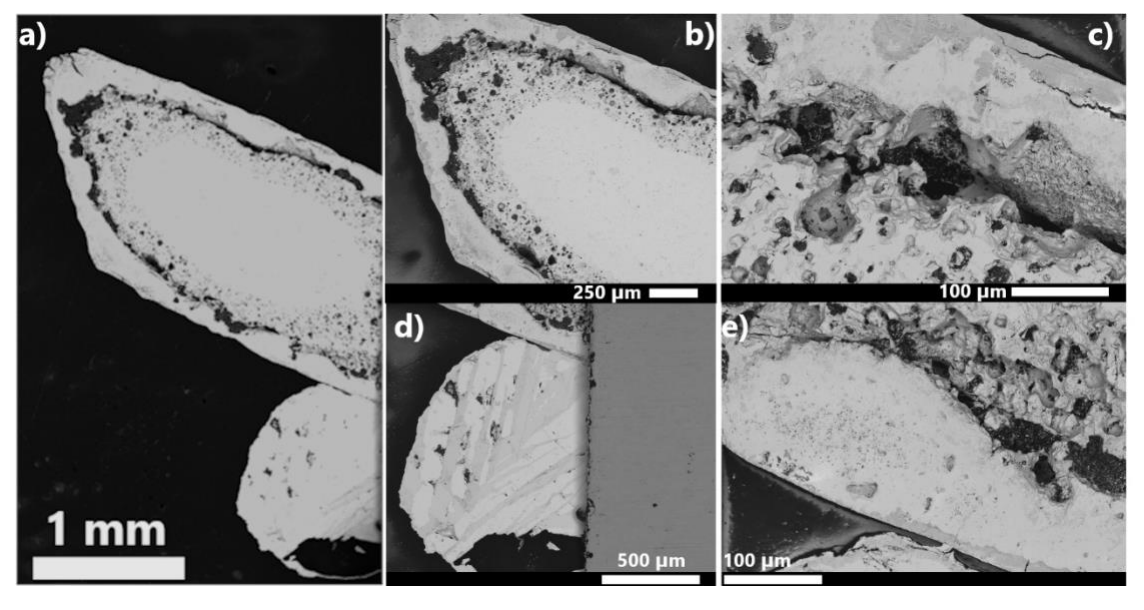


Figure 7. Backscattered electron micrographs of the cross section of a, b) a piece of Yb_{13.7}Lu_{0.3}MnSb₁₁ after oxidation in the TG/DSC, c) a closer look at the outer shell and porous region, d) a closer look at the ball of melted material, and e) a closer look at the interface between the ball of melted material (coming from the bottom) and the main piece of material.

In addition to backscattered electron microscopy, the oxidized sample was analyzed using energy dispersive spectroscopy (EDS). The elemental maps obtained from EDS are shown in Figure 8a) – f). The mapping of Yb, Mn, and Lu showed an even distribution of the elements across both the shell and interior of the sample. The Sb seems to be concentrated within the core of the sample with the outer shell being relatively Sb deficient except for several streaks on the outer shell where it meets the void region. The oxygen seems to be concentrated in the outer shell of the sample with the inner core showing relatively low concentrations. Moving to the ball of melted material (Figure 8g) – 1)), the same striations seen in the backscattered electron micrographs appears in the Yb, Mn, and Sb maps suggesting this is a eutectic melt of the three elements. EDS on single points of the melted ball showed it to be consistent with YbSb2 and YbMnSb2.

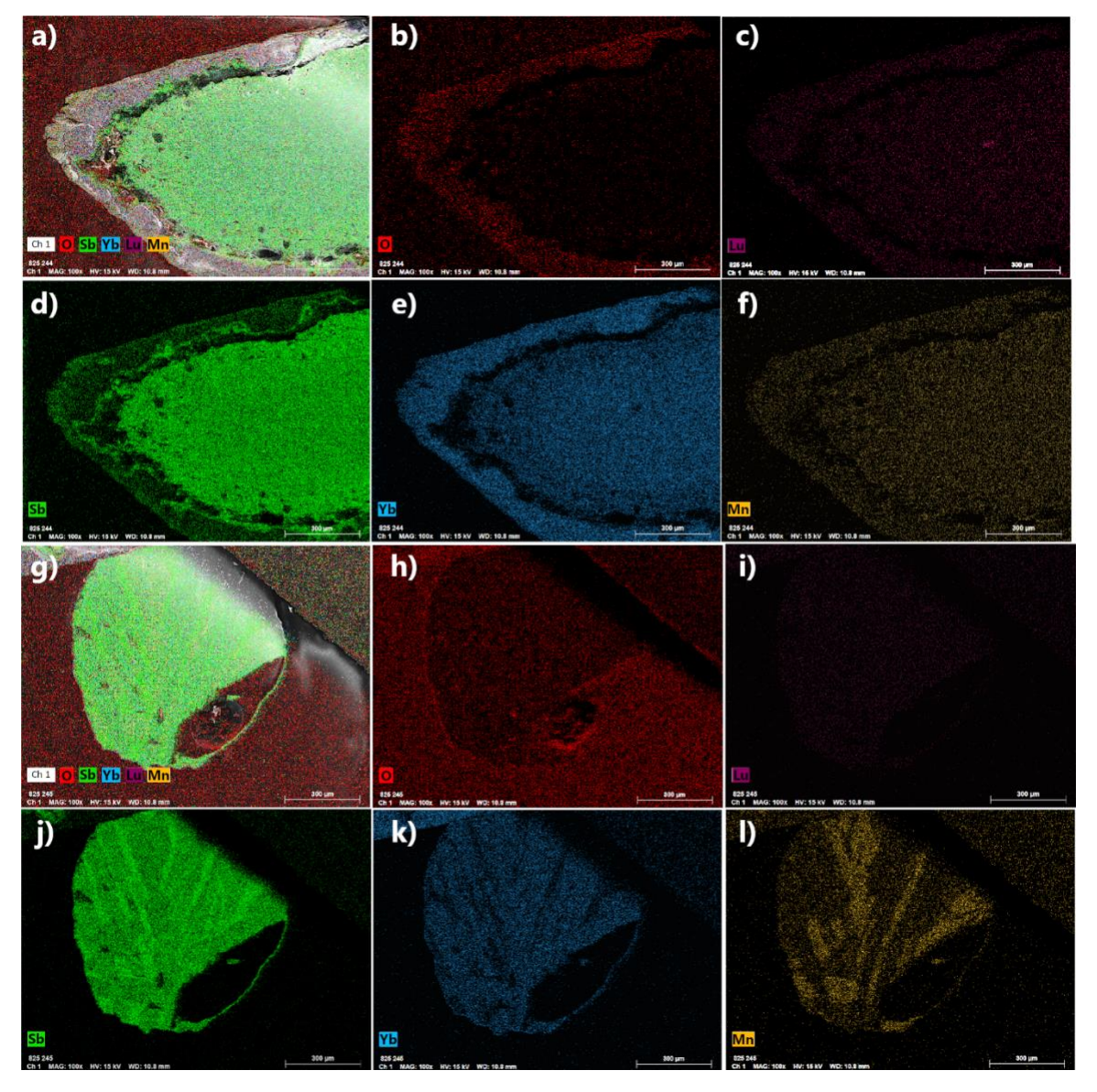


Figure 8. a) – f) Elemental mapping of the oxidized piece of Yb_{13.7}Lu_{0.3}MnSb₁₁ obtained using energy dispersive spectroscopy. a) shows the combined map over a secondary electron micrograph, b) shows O in red, c) shows Lu in purple, d) shows Sb in green, e) shows Yb in blue, and f) shows Mn in gold. All scale bars are 300 μm. g) – h) Elemental mapping of the material that melted from the oxidized piece of Yb_{13.7}Lu_{0.3}MnSb₁₁ obtained using energy dispersive spectroscopy. g) shows the combined map over a secondary electron micrograph, h) shows O in red, i) shows Lu in purple, j) shows Sb in green, k) shows Yb in blue, and l) shows Mn in gold. All scale bars are 300 μm.

To see how this oxide shell formation changes when performed on a larger scale, an entire pellet (12.7 mm diameter, ~3 mm thick) was oxidized directly in a box furnace by heating to 1000°C at 200°C / hour and dwelling there for 12 hours under ambient atmospheric conditions. Before and after photos of the pellet can be seen in Figure 9. Much like in the TG/DSC experiment, the sample of Yb_{13.7}Lu_{0.3}MnSb₁₁ starts as a black polished material and after oxidation the pellet has developed a glossy brownish-black outer shell along with a mass of black material which appears to have melted out of the sample. Unlike what was seen in the TG/DSC experiments, there is extensive cracking of this outermost shell, especially where the black material has melted out. The only significant reaction between the Al₂O₃ holder and the sample was where the material which melted out contacted the Al₂O₃. At this region the black material was fused to the Al₂O₃.



Figure 9. a) Before and b - d) after pictures of the pellet of Yb_{13.7}Lu_{0.3}MnSb₁₁ oxidized at 1000°C for 12 hours under ambient atmospheric conditions.

Figure 10 shows backscattered electron micrographs of the cross section of the oxidized pellet. In Figure 10 a) the overall structure of the oxidized pellet can be seen to consist of an outer shell, a porous void section, and an inner core. In Figure 10 b), a \sim 100 μ m thick layer between the inner core and porous region can be seen. A closer view of the outer shell can be seen in Figure 10 c). This shows a dark outer shell which extends \sim 90 μ m below the surface. Below that a thin band of another material can be seen in patches. Before the porous region, there is an additional 100 μ m thick band of lighter material which is attached to the outer shell.

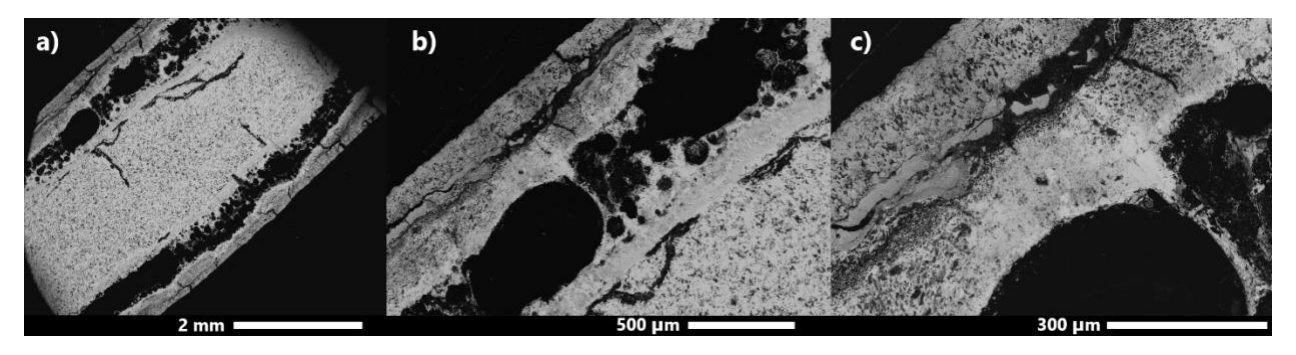


Figure 10. Backscattered electron micrographs of the cross section of the oxidized Yb₁₄₋ $_x$ Lu $_x$ MnSb₁₁ pellet a) as a whole, and b), c) closer views of the outer shell.

The other half of the oxidized pellet was carefully dissected to perform PXRD on the individual components. Figure 11 shows the sample and the PXRD pattern from the glossy outer shell after being removed and ground. The PXRD shows that the shell consists mostly of Yb₂O₃ along with small amounts of YbMnSb₂, YbSb₂, and Sb. The presence of these Sb rich phases along with elemental Sb suggests that this outer layer forms from the oxidation of YbSb₂ and YbMnSb₂ to Yb₂O₃ and a Mn oxide which is likely in such small amounts it is not easily visible by PXRD. It is possible the unindexed peak at 31° two theta is a Mn containing oxide or Mn-Sb-O ternary phase (or something more complicated), but no reported phases fit the full diffraction pattern well. Along with forming those oxides, elemental Sb is formed which likely acts as a flux to help the growth of the outer shell and helps to explain the glossy appearance. At high temperatures most of the Sb likely sublimes as Sb₄O₆ after oxidation, but small amounts remain trapped under the surface as seen in the backscattered electron micrograph (Figure 10 c)).

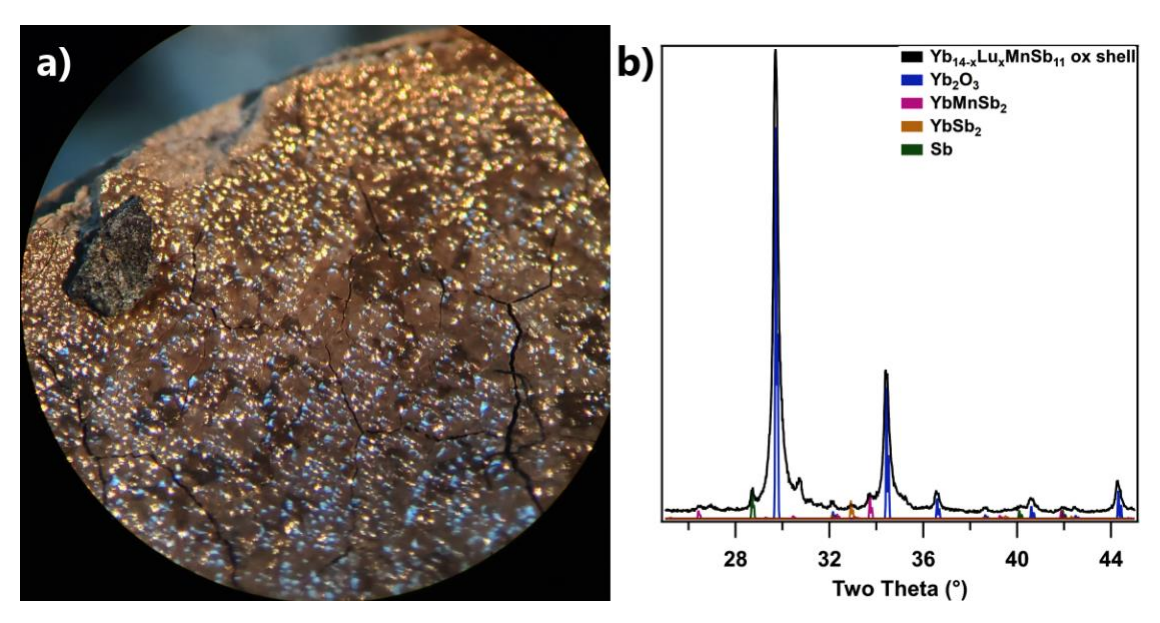


Figure 11. a) a picture of the glossy outer shell, and b) a PXRD pattern of the shell after being removed and ground.

Figure 12 shows the PXRD pattern of the black material which appeared to melt out of the sample and attach itself to the Al₂O₃ holder. The diffraction pattern was indexed as YbSb₂, YbMnSb₂, Yb₂O₃, and Sb. The YbSb₂ showed heavy preferred orientation with an overexpression of high k miller indices such as the (0 10 1) reflection around 60° two theta seen in Figure 12 a) and the (0 6 0) reflection around 32° two theta seen in Figure 12 b). This is likely a result of the asymmetric orthorhombic lattice parameters of YbSb₂, a = 4.536 Å, b = 16.63 Å, c = 4.271 Å.

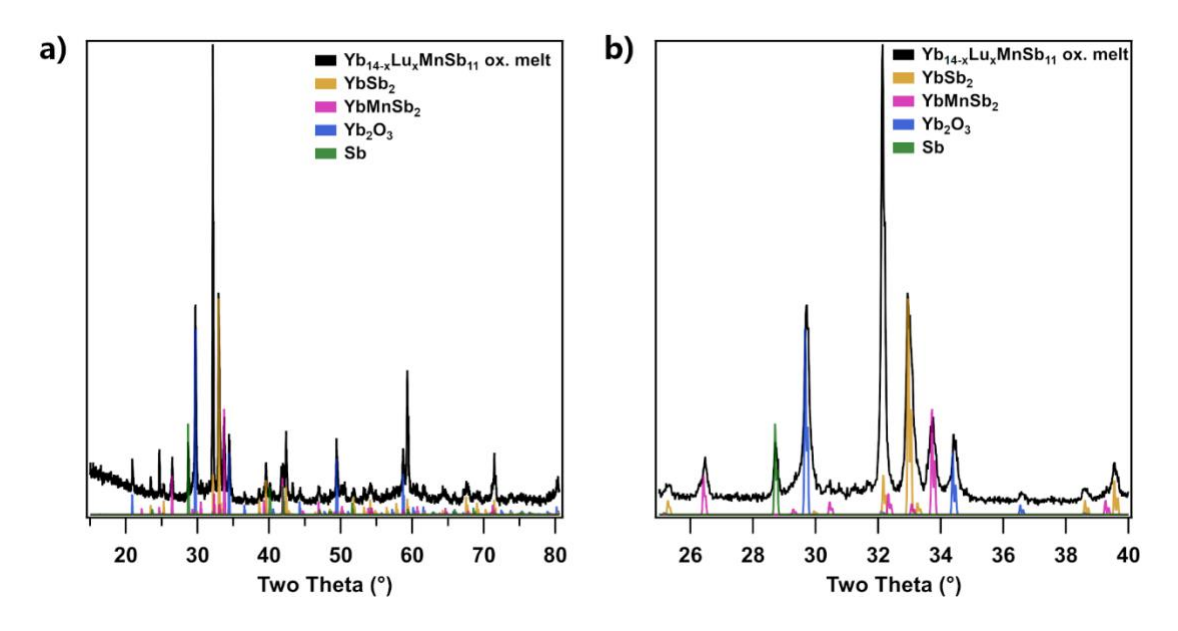


Figure 12. PXRD patterns of the melted material at a) the full range of two theta and b) a zoomed in view.

A PXRD diffraction pattern of the interior pellet and porous region can be seen in Figure 13. This region consisted of Yb_{13.7}Lu_{0.7}MnSb₁₁, Yb₁₁Sb₁₀, YbSb, YbMnSb₂, YbSb₂, Yb₂O₃, and Sb. Because the melted portion contained YbSb₂, YbMnSb₂, Yb₂O₃, and Sb, it can be assumed that those come mostly from the porous region which remained attached to the inner core. The YbSb is likely the band of material which was seen between the porous region and the core. This was not seen in the oxidation of undoped Yb₁₄MnSb₁₁ and it is likely this phase is stabilized by the presence of the trivalent Lu. The Yb₁₁Sb₁₀ and Yb_{13.97}Lu_{0.3}MnSb₁₁ make up the core of the sample. As seen in the EDS of the sample oxidized in the TG/DSC, the oxygen and in turn Yb₂O₃ is mostly localized to the outer region with the inner core showing much lower amounts.

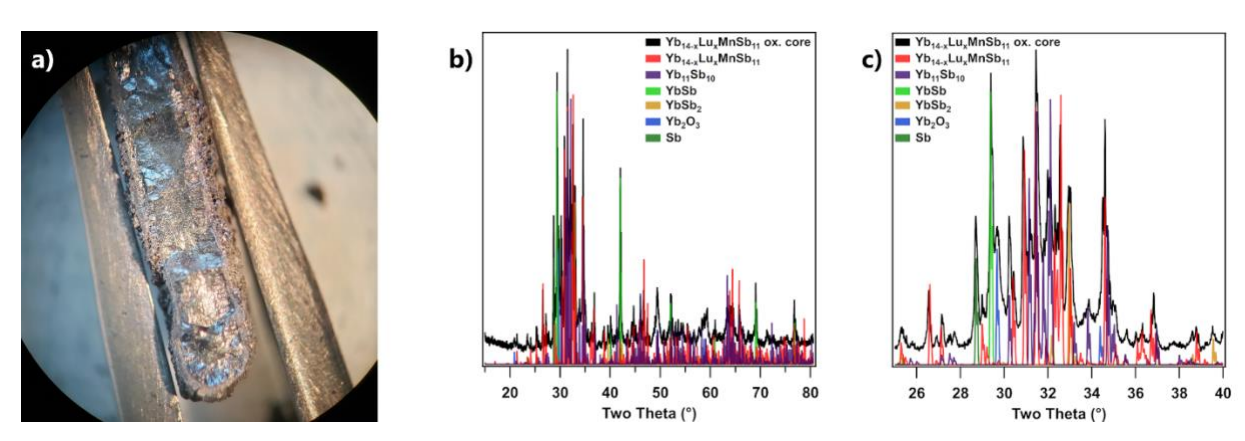


Figure 13. a) A picture of the core section of the oxidized Yb_{13.7}Lu_{0.3}MnSb₁₁, b) a full PXRD pattern of the core material after being ground, and c) a zoomed in view of the 25° to 40° two theta range where many of the phases have intense reflections.

While the formation and melting of YbSb₂ and YbMnSb₂ proved problematic in high temperature oxidation whether the sample was doped with Lu or not, it may be possible that Lu does help in quickly forming a passivating oxide shell at lower temperatures. This has implications for the ease of processing these kinds of materials in large batches for a device as some processes require elevated temperatures. To investigate the potential for better low temperature passivation, a piece of Yb₁₄MnSb₁₁ and a piece of Yb_{13.7}Lu_{0.3}MnSb₁₁ were both cycled from room temperature to 400 °C four times under a flow of dry air while being monitored using TG/DSC. The before and after photos of the Yb₁₄MnSb₁₁ (Figure 14 a), b)) and

Yb_{14-x}Lu_xMnSb₁₁ (Figure 14 c), d)) are shown below. In both cases, the samples start as shiny black materials and after the low temperature oxidation, both samples have developed a noticeable film which interferes with visible light causing a green appearance at certain angles. The TG/DSC for this oxidation cycling can be seen in Figure 14 e). Both samples gain less than 0.5% of their starting mass with the Lu doped sample gaining slightly less (0.432% in comparison to 0.472%). This difference is likely due to slight differences in surface area of the samples. In the DSC, the sample of Yb₁₄MnSb₁₁ shows relatively large, sweeping exotherms which increase in magnitude with cycling. This may be due to an increase in reactions occurring as oxygen diffuses further into the sample. The DSC for the low temperature oxidation of the sample of Yb_{13.7}Lu_{0.3}MnSb₁₁ shows much smaller sweeping exotherms with the third cycle from room temperature to 400 °C showing a flat DSC signal. However, the cycle after that shows a return to the sweeping exotherm along with a large relative mass gain in comparison to the previous three cycles. This may suggest that the passivating oxide film formed may crack over time. Figure 14 f) shows the PXRD patterns of the sample of Yb14MnSb11 and Yb13.7Lu0.3MnSb11 after four cycles to 400 °C under a flow of dry air. The sample of Yb₁₄MnSb₁₁ showed 81.43(14) wt% Yb₁₄MnSb₁₁, 13.55(11) wt% Yb₁₁Sb₁₀, 4.16(7) wt% Yb₂O₃, and 0.86(5) wt% Sb (GoF:1.61, Rp: 6.89, wRp: 9.17). In comparison to that, the Lu doped sample was found to contain 95.96(11) wt% Yb₁₄MnSb₁₁, 3.24(11) wt% Yb₂O₃, and 0.80(4) wt% Sb. The notable lack of Yb₁₁Sb₁₀ suggests that the oxide shell formed helps to passivate the sample from oxygen diffusion into the core as this phase was only seen in the core of the heavily oxidized samples. The presence of Sb in these samples supports the idea that the oxidation of these materials occurs through the oxidation of Yb, Lu, and Mn forming more Sb rich phases until all metals have been converted to oxides and only Sb is left.

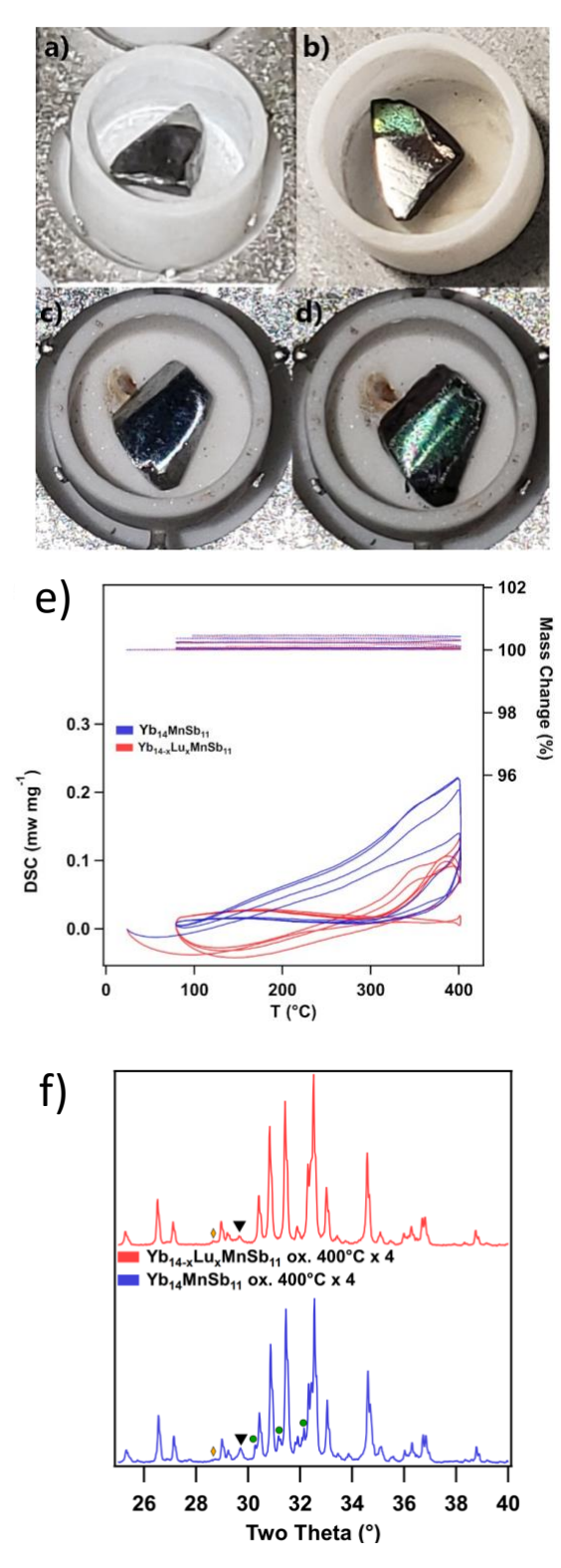


Figure 14. Pictures of Yb₁₄MnSb₁₁ (a), b)) and Yb_{13.7}Lu_{0.3}MnSb₁₁ (c), d)) before and after four cycles to 400 °C under a flow of dry air. e) TG/DSC of Yb₁₄MnSb₁₁ and Yb_{13.7}Lu_{0.3}MnSb₁₁ during four cycles to 400 °C under a flow of dry air. f) PXRD patterns of Yb₁₄MnSb₁₁ (bottom,

blue) and Yb_{13.7}Lu_{0.3}MnSb₁₁ (top, red) after 4 cycles to 400 °C under a flow of dry air. Reflections from Yb₂O₃ are marked by the black triangle, Yb₁₁Sb₁₀ by the green circles and Sb by the orange diamond.

Conclusions

Lu substitution in Yb₁₄MnSb₁₁ effectively lowers the carrier concentration, like other RE solid solutions of Yb₁₄MnSb₁₁. ^{16–18,20} The solubility of Lu within Yb₁₄MnSb₁₁ seems to be limited with LuSb precipitates forming at *x* = 0.5 and above. Overall, this lowering of carrier concentrations decreases the peak *zT* of the Yb_{14-x}Lu_xMnSb₁₁ series in comparison to the pristine compound as predicted by recent modeling of the transport properties in Yb₁₄Mg_{1-x}Al_xSb₁₁. ⁹ Oxidation of Yb_{14-x}Lu_xMnSb₁₁ at high temperatures showed the formation of molten YbSb₂ and YbMnSb₂, similar to what has been shown for the pristine compound. Oxidation at moderate temperatures suggests that Lu substitution may help to form a stable passivating coating. Further oxidation studies employing Sc and Y, as more electropositive elements may provide better stability through stronger RE-O bonds while also providing a uniform (Yb,RE)₂O₃ coating.

Supporting Information

Supporting Information is available free of charge at https://pubs.acs.org/doi/ Contains: PXRD's of Yb4Sb3, MnSb, and YbH2, Rietveld refinement of PXRD patterns of Yb14xLuxMnSb11, Temperature dependent Hall carrier concentration and mobility.

Acknowledgements

The research was supported by NSF DMR-2001156 and performed in part at the Jet Propulsion Laboratory, California Institute of Technology under contract with the NASA Science Missions Directorate's Radioisotope Power Systems Program. The Advanced Materials Characterization and Testing laboratory (AMCaT) supported by NSF DMR-1725618 at University of California, Davis was accessed for the SEM/EDS data. SEM samples were carbon coated in the Center for Nano-MicroManufacturing (CNM2) at UC Davis.

References

- (1) Morton, E. Lucy Mission https://blogs.nasa.gov/lucy/ (accessed Oct 9, 2022).
- (2) Duda, L.; Shekhtman, S. NASA Troubleshoots Asteroid-Bound Lucy Across Millions of Miles | NASA https://www.nasa.gov/feature/goddard/2022/nasa-team-troubleshoots-asteroid-bound-lucy-across-millions-of-miles (accessed Oct 9, 2022).
- (3) Mason, L. S. Realistic Specific Power Expectations for Advanced Radioisotope Power Systems. *J. Propuls. Power* **2007**, *23* (5), 1075–1079. https://doi.org/10.2514/1.26444.
- (4) Mahan, G. D. Introduction to Thermoelectrics. *APL Mater.* **2016**, *4* (10), 104806. https://doi.org/10.1063/1.4954055.
- (5) Beretta, D.; Neophytou, N.; Hodges, J. M.; Kanatzidis, M. G.; Narducci, D.; Martin-Gonzalez, M.; Beekman, M.; Balke, B.; Cerretti, G.; Tremel, W.; et al. Thermoelectrics: From History, a Window to the Future. *Mater. Sci. Eng. R Reports* **2019**, *138* (July 2018), 100501. https://doi.org/10.1016/j.mser.2018.09.001.
- (6) He, A.; Wille, E. L. K.; Moreau, L. M.; Thomas, S. M.; Lawrence, J. M.; Bauer, E. D.; Booth, C. H.; Kauzlarich, S. M. Intermediate Yb Valence in the Zintl Phases Yb₁₄MSb₁₁ (M = Zn, Mn, Mg): XANES, Magnetism, and Heat Capacity. *Phys. Rev. Mater.* **2020**, *4* (11), 114407. https://doi.org/10.1103/PhysRevMaterials.4.114407.
- (7) Hanus, R.; George, J.; Wood, M.; Bonkowski, A.; Cheng, Y.; Abernathy, D. L.; Manley, M. E.; Hautier, G.; Snyder, G. J.; Hermann, R. P. Uncovering Design Principles for Amorphous-like Heat Conduction Using Two-Channel Lattice Dynamics. *Mater. Today Phys.* **2021**, *18*, 100344. https://doi.org/10.1016/j.mtphys.2021.100344.
- (8) Bernges, T.; Hanus, R.; Wankmiller, B.; Imasato, K.; Lin, S.; Ghidiu, M.; Gerlitz, M.; Peterlechner, M.; Graham, S.; Hautier, G.; et al. Considering the Role of Ion Transport in Diffuson-Dominated Thermal Conductivity. *Adv. Energy Mater.* **2022**, 2200717. https://doi.org/10.1002/aenm.202200717.
- (9) Perez, C. J.; Wood, M.; Ricci, F.; Yu, G.; Vo, T.; Bux, S. K.; Hautier, G.; Rignanese, G.-M.; Snyder, G. J.; Kauzlarich, S. M. Discovery of Multivalley Fermi Surface Responsible for the High Thermoelectric Performance in Yb₁₄MnSb₁₁ and Yb₁₄MgSb₁₁. *Sci. Adv.* **2021**, 7 (4), eabe9439. https://doi.org/10.1126/sciadv.abe9439.
- (10) Xin, J.; Tang, Y.; Liu, Y.; Zhao, X.; Pan, H.; Zhu, T. Valleytronics in Thermoelectric Materials. *npj Quantum Mater.* **2018**, *3* (1), 9. https://doi.org/10.1038/s41535-018-0083-6.
- (11) Justl, A. P.; Cerretti, G.; Bux, S. K.; Kauzlarich, S. M. 2 + 2 = 3: Making Ternary Phases through a Binary Approach. *Chem. Mater.* **2022**, *34* (3), 1342–1355. https://doi.org/10.1021/acs.chemmater.1c04031.
- (12) Grebenkemper, J. H.; Hu, Y.; Barrett, D.; Gogna, P.; Huang, C.-K.; Bux, S. K.; Kauzlarich, S. M. High Temperature Thermoelectric Properties of Yb₁₄MnSb₁₁ Prepared from Reaction of MnSb with the Elements. *Chem. Mater.* **2015**, *27* (16), 5791–5798. https://doi.org/10.1021/acs.chemmater.5b02446.
- (13) Brandon, E.; Caillat, T.; Fleurial, J.-P.; Ewell, R.; Li, B.; Firdosy, S.; Paik, J.-A.; Nakatsukasa, G.; Huang, C.-K.; Nesmith, B.; et al. Development of New High Temperature Power Generating Couples for the Advanced Thermoelectric Converter (ATEC). In *40th International Conference on Environmental Systems*; American Institute of Aeronautics and Astronautics: Reston, Virigina, 2010; pp 1–7. https://doi.org/10.2514/6.2010-7004.
- (14) Ravi, V.; Firdosy, S.; Caillat, T.; Brandon, E.; Van Der Walde, K.; Maricic, L.; Sayir, A. Thermal Expansion Studies of Selected High-Temperature Thermoelectric Materials. *J.*

- Electron. Mater. 2009, 38 (7), 1433–1442. https://doi.org/10.1007/S11664-009-0734-2.
- (15) Vasilyeva, I.; Abdusalyamova, M.; Makhmudov, F.; Eshov, B.; Kauzlarich, S. Thermal Air-Oxidized Coating on Yb_{14-x}RE_xMnSb₁₁ Ceramics. *J. Therm. Anal. Calorim.* **2019**, *136* (2), 541–548. https://doi.org/10.1007/s10973-018-7659-z.
- (16) Grebenkemper, J. H.; Klemenz, S.; Albert, B.; Bux, S. K.; Kauzlarich, S. M. Effects of Sc and Y Substitution on the Structure and Thermoelectric Properties of Yb₁₄MnSb₁₁. *J. Solid State Chem.* **2016**, *242*, 55–61. https://doi.org/10.1016/j.jssc.2016.03.015.
- (17) Hu, Y.; Bux, S. K.; Grebenkemper, J. H.; Kauzlarich, S. M. The Effect of Light Rare Earth Element Substitution in Yb₁₄MnSb₁₁ on Thermoelectric Properties. *J. Mater. Chem. C* **2015**, *3* (40), 10566–10573. https://doi.org/10.1039/c5tc02326b.
- (18) Uvarov, C. A.; Abdusalyamova, M. N.; Makhmudov, F.; Star, K.; Fleurial, J.-P.; Kauzlarich, S. M. The Effect of Tm Substitution on the Thermoelectric Performance of Yb₁₄MnSb₁₁. *Sci. Adv. Mater.* **2011**, *3* (4), 652–658. https://doi.org/10.1166/sam.2011.1196.
- (19) Yu, C.; Chen, Y.; Xie, H.; Snyder, G. J.; Fu, C.; Xu, J.; Zhao, X.; Zhu, T. Improved Thermoelectric Properties in Lu-Doped Yb₁₄MnSb₁₁ Zintl Compounds. *Appl. Phys. Express* **2012**, *5* (3), 031801. https://doi.org/10.1143/APEX.5.031801.
- (20) Devlin, K. P.; Grebenkemper, J. H.; Lee, K.; Cerretti, G.; Bux, S. K.; Kauzlarich, S. M. Enhancement of the Thermal Stability and Thermoelectric Properties of Yb₁₄MnSb₁₁ by Ce Substitution. *Chem. Mater.* **2020**, *32* (21), 9268–9276. https://doi.org/10.1021/acs.chemmater.0c03043.
- Justl, A. P.; Kauzlarich, S. M. Probing High-Temperature Oxidation of Thermoelectric Phases Yb₁₄MSb₁₁ (M = Mg, Mn, Zn). *ACS Appl. Mater. Interfaces* **2022**, *14* (41), 47246–47254. https://doi.org/10.1021/acsami.2c13093.
- (22) Devlin, K. P.; Grebenkemper, J. H.; Lee, K.; Cerretti, G.; Bux, S. K.; Kauzlarich, S. M. Enhancement of the Thermal Stability and Thermoelectric Properties of Yb₁₄MnSb₁₁ by Ce Substitution. *Chem. Mater.* **2020**, *32* (21), 9268–9276. https://doi.org/10.1021/acs.chemmater.0c03043.
- (23) Petříček, V.; Dušek, M.; Palatinus, L. Crystallographic Computing System JANA2006: General Features. *Zeitschrift für Krist. Cryst. Mater.* **2014**, *229* (5), 345–352. https://doi.org/10.1515/zkri-2014-1737.
- (24) Perez, C. J.; Cerretti, G.; Wille, E. L. K.; Devlin, K. P.; Grewal, N. S.; Justl, A. P.; Wood, M.; Bux, S. K.; Kauzlarich, S. M. Evolution of Thermoelectric Properties in the Triple Cation Zintl Phase: Yb_{13-x}Ca_xBaMgSb₁₁ (x = 1-6). *Chem. Mater.* **2021**, *33* (20), 8059–8069. https://doi.org/10.1021/acs.chemmater.1c02584.
- (25) Justl, A. P.; Cerretti, G.; Bux, S. K.; Kauzlarich, S. M. Hydride Assisted Synthesis of the High Temperature Thermoelectric Phase: Yb₁₄MgSb₁₁. *J. Appl. Phys.* **2019**, *126* (16), 165106. https://doi.org/10.1063/1.5117291.
- (26) Hu, Y.; Wang, J.; Kawamura, A.; Kovnir, K.; Kauzlarich, S. M. Yb₁₄MgSb₁₁ and Ca₁₄MgSb₁₁ New Mg-Containing Zintl Compounds and Their Structures, Bonding, and Thermoelectric Properties. *Chem. Mater.* **2015**, *27* (1), 343–351. https://doi.org/10.1021/cm504059t.
- (27) Wood, C.; Zoltan, D.; Stapfer, G. Measurement of Seebeck Coefficient Using a Light Pulse. *Rev. Sci. Instrum.* **1985**, *56* (5), 719–722. https://doi.org/10.1063/1.1138213.
- (28) Borup, K. A.; Toberer, E. S.; Zoltan, L. D.; Nakatsukasa, G.; Errico, M.; Fleurial, J.-P.; Iversen, B. B.; Snyder, G. J. Measurement of the Electrical Resistivity and Hall

- Coefficient at High Temperatures. *Rev. Sci. Instrum.* **2012**, *83* (12), 123902. https://doi.org/10.1063/1.4770124.
- (29) Samsonov, G. V.; Abdusalyamova, M. N.; Shokirov, K.; Pryakhina, S. A. Physicochemical Properties of the Rare Earth Monoantimonides. *Neorg. Mater.* **1974**, *10* (11), 1951–9154.
- (30) Hu, Y.; Chen, C. W.; Cao, H.; Makhmudov, F.; Grebenkemper, J. H.; Abdusalyamova, M. N.; Morosan, E.; Kauzlarich, S. M. Tuning Magnetism of [MnSb4]⁹⁻ Cluster in Yb14MnSb11 through Chemical Substitutions on Yb Sites: Appearance and Disappearance of Spin Reorientation. *J. Am. Chem. Soc.* **2016**, *138* (38), 12422–12431. https://doi.org/10.1021/jacs.6b05636.
- (31) Newbury, D. E.; Ritchie, N. W. M. Is Scanning Electron Microscopy/Energy Dispersive X-Ray Spectrometry (SEM/EDS) Quantitative? *Scanning* **2013**, *35* (3), 141–168. https://doi.org/10.1002/sca.21041.
- (32) Pavlosiuk, O.; Kleinert, M.; Swatek, P.; Kaczorowski, D.; Wiśniewski, P. Fermi Surface Topology and Magnetotransport in Semimetallic LuSb. *Sci. Rep.* **2017**, *7* (1), 12822. https://doi.org/10.1038/s41598-017-12792-8.

TOC

